

# UCLA

## UCLA Previously Published Works

### Title

Plant-expressed virus-like particles reveal the intricate maturation process of a eukaryotic virus

### Permalink

<https://escholarship.org/uc/item/5qc7k0sr>

### Journal

Communications Biology, 4(1)

### ISSN

2399-3642

### Authors

Castells-Graells, Roger  
Ribeiro, Jonas RS  
Domitrovic, Tatiana  
et al.

### Publication Date








2021

### DOI

10.1038/s42003-021-02134-w

Peer reviewed

## Plant-expressed virus-like particles reveal the intricate maturation process of a eukaryotic virus

Roger Castells-Graells <sup>1,5</sup>, Jonas R. S. Ribeiro<sup>2</sup>, Tatiana Domitrovic<sup>2</sup>, Emma L. Hesketh <sup>3</sup>,  
Charlotte A. Scarff <sup>3</sup>, John E. Johnson <sup>4</sup>, Neil A. Ranson <sup>3</sup>, David M. Lawson <sup>1</sup> &  
George P. Lomonossoff <sup>1</sup>✉

Many virus capsids undergo exquisitely choreographed maturation processes in their host cells to produce infectious virions, and these remain poorly understood. As a tool for studying virus maturation, we transiently expressed the capsid protein of the insect virus *Nudaurelia capensis* omega virus (N $\omega$ V) in *Nicotiana benthamiana* and were able to purify both immature procapsids and mature capsids from infiltrated leaves by varying the expression time. Cryo-EM analysis of the plant-produced procapsids and mature capsids to 6.6 Å and 2.7 Å resolution, respectively, reveals that in addition to large scale rigid body motions, internal regions of the subunits are extensively remodelled during maturation, creating the active site required for autocatalytic cleavage and infectivity. The mature particles are biologically active in terms of their ability to lyse membranes and have a structure that is essentially identical to authentic virus. The ability to faithfully recapitulate and visualize a complex maturation process in plants, including the autocatalytic cleavage of the capsid protein, has revealed a ~30 Å translation-rotation of the subunits during maturation as well as conformational rearrangements in the N and C-terminal helical regions of each subunit.

<sup>1</sup>Department of Biological Chemistry, John Innes Centre, Colney, UK. <sup>2</sup>Virology Department, Instituto de Microbiologia Paulo de Goes, Universidade Federal do Rio de Janeiro, Rio de Janeiro, Brazil. <sup>3</sup>Astbury Centre for Structural Molecular Biology, School of Molecular & Cellular Biology, Faculty of Biological Sciences, University of Leeds, Leeds, UK. <sup>4</sup>Department of Integrative Structural and Computational Biology, The Scripps Research Institute, La Jolla, CA, USA. <sup>5</sup>Present address: Department of Chemistry and Biochemistry, University of California, Los Angeles, CA, USA. ✉email: [george.lomonossoff@jic.ac.uk](mailto:george.lomonossoff@jic.ac.uk)

Maturation is a critical part of the replication cycle of all animal and bacterial viruses studied to date and is required for the production of infectious virions. The outlines of maturation have been determined for retroviruses<sup>1</sup>, flaviviruses<sup>2</sup>, herpesvirus<sup>3</sup> and a variety of other viruses, but detailed mechanistic studies have not been reported. The maturation of particles of the insect virus, *Nudaurelia capensis* omega virus (N $\omega$ V), has been studied extensively in vitro. As a result, the virus is now an exemplar for maturation processes<sup>4,5</sup>. N $\omega$ V belongs to the *Alphatetraviridae*, a family of insect viruses with non-enveloped  $T=4$  capsids that infect a single order of insects, the Lepidoptera<sup>6,7</sup>. N $\omega$ V has a single-stranded positive-sense, bipartite RNA genome consisting of RNA-1 (~5.3 kb), that encodes the RNA-dependent RNA polymerase, and RNA-2 (~2.5 kb), that encodes the 70 kDa  $\alpha$  capsid protein<sup>8</sup>. When the coat protein of N $\omega$ V is expressed in insect cells, it assembles into stable intermediate virus-like particles (VLPs) (known as the procapsid), 48 nm in diameter, that are porous at neutral pH (pH 7.6)<sup>9</sup>. These particles undergo a maturation process when they are exposed to acidic conditions (pH 5.0) in vitro. This involves large-scale subunit reorganisation and an autocatalytic cleavage of the  $\alpha$  capsid protein between residues Asn570 and Phe571 to give two polypeptides,  $\beta$  and  $\gamma$ , of 62- and 8-kDa, respectively, that remain as part of the mature particle (Fig. S1). The resulting mature particles are 42 nm in diameter, and they are morphologically indistinguishable from the authentic virus<sup>10</sup>. Lowering the pH of a procapsid preparation from 7.6 to 5.0 results in rapid, large-scale, conformational changes of the subunits and maturation<sup>11</sup>; however, intermediate capsid states can be detected at pH values maintained between 7.6 and 5.0<sup>12</sup>. These conformational changes are reversible at elevated pH if no more than 10% of the subunits have been cleaved or in the mutant Asn570Thr, which is incapable of effecting the cleavage<sup>12,13</sup>.

The  $\gamma$  peptide acts as a lytic peptide, providing an effective mechanism to breach a membrane and allowing non-enveloped animal viruses to enter cells<sup>14</sup>. Experiments using liposomes loaded with a self-quenching dye, and N $\omega$ V VLPs at different stages in the maturation (pH 7.6–5.0), have shown that the maximum lytic activity occurs at alkaline pH (pH 7.5 and above) and that it is necessary for the  $\gamma$  peptide to be released for this activity<sup>15,16</sup>. Therefore, procapsid VLPs, in which the  $\alpha$  peptide is not cleaved, do not lyse liposomes<sup>16</sup>. This pH-dependent functionality of the lytic peptide is believed to correlate with the uptake of virus particles under the alkaline conditions of the insect gut<sup>17</sup>.

Though comparison of the structures of procapsids and capsids produced by expression in insect cells and subsequent in vitro maturation have been very revealing, they have led to only an understanding of the gross structural changes that accompany the process. Furthermore, they rely on the assumption that maturation by reducing pH follows an identical pathway to that which occurs within cells. While this is reasonable, given that structures of capsids matured in vitro are indistinguishable from authentic virions isolated from infected insects, it is possible that the pathway may be different within cells. However, maturation of capsids within insect cells has not been observed, rendering in vivo studies impossible in this system.

Plants are a highly effective system for producing VLPs<sup>18–23</sup>. In most instances, expression of the coat protein subunits alone results in the assembly of VLPs; however, in the case of members of the order *Picornavirales*, where coat protein cleavage is required for particle assembly, co-expression of a virus-encoded protease is also required<sup>20,22</sup>. To date, the resulting purified VLPs have been mature, static structures, which closely resemble the original virion both in structure and immunogenicity.

To explore whether plant-based systems can be used to visualize the molecular details of the maturation processes, we transiently expressed the coat protein subunit of N $\omega$ V and show that the cleavage associated with maturation occurs within the cells. It proved possible to purify both procapsids and capsids from leaf tissue by varying the time at which the VLPs were extracted. Using cryo-EM, we solved the structure of the procapsids and capsids to 6.6 and 2.7 Å resolution, respectively, and showed that the plant-produced mature capsids have the ability to lyse liposomes and are essentially identical in structure to authentic virus. Comparison of the structures of the plant-produced procapsids and capsids revealed that, in addition to large scale rigid body motions, internal regions of the subunits are extensively remodelled during maturation, creating the active site required for autocatalytic cleavage and infectivity.

## Results

**Expression and purification of N $\omega$ V VLPs in plants.** The N $\omega$ V WT coat protein gene, codon-optimised for *N. benthamiana*, was inserted into plasmid pEAQ-*HT*<sup>24</sup> to give plasmid pEAQ-*HT*-N $\omega$ V-WT. Expression of the coat protein was initiated by infiltrating leaves of *N. benthamiana* with suspensions of *A. tumefaciens* harbouring pEAQ-*HT*-N $\omega$ V-WT followed by the collection of leaf disks various days post-infiltration (dpi). Western blot analysis of total protein extracts using a polyclonal antibody specific for the N $\omega$ V coat protein showed that expression of the 70 kDa full-length coat protein ( $\alpha$  protein) was first detected at 2 dpi (Fig. 1a). By 3–4 dpi a lower molecular weight band of about 62 kDa, consistent with the size of the  $\beta$  protein, appeared suggesting that the full-length N $\omega$ V coat protein undergoes processing over time within the plant tissue. Additionally, higher molecular weight bands of around 150 kDa were observed in the extracts from later time points, suggestive of the formation of dimers, whether covalently linked or just SDS-resistant, of the coat protein. The identity of these bands as consisting of N $\omega$ V coat protein was confirmed by mass spectrometry of tryptic digests of the purified proteins.

To confirm that VLPs are, indeed, produced in plant cells, thin sections were prepared from leaves 8 days after infiltration with either pEAQ-*HT* (empty vector) or pEAQ-*HT*-N $\omega$ V-WT and examined by TEM. Large numbers of particles, characteristic of N $\omega$ V VLPs, could be seen in the cytoplasm of cells from leaves infiltrated with pEAQ-*HT*-N $\omega$ V-WT (Fig. 1c, d) but not in cells from tissue infiltrated with the empty vector (Fig. 1b). This, coupled with the time-dependent cleavage of the  $\alpha$  protein, indicates that the expressed N $\omega$ V coat protein subunits assemble into procapsids that are able to mature within plant cells.

To characterise the particles produced in plants, VLPs were extracted at pH 7.6 either 3–4 dpi to maximise the level of procapsids<sup>25</sup> or at 8 dpi to isolate mature capsids. Both types of capsid particle were purified by centrifugation through continuous gradients (10–40% (w/v) sucrose for procapsids, and 10–50% (w/v) Optiprep for mature capsids), and the protein content of the fractions was analysed by SDS-PAGE (Fig. S2). Fractions containing the uncleaved  $\alpha$  protein and the cleaved  $\beta$  protein were pooled separately to give samples of purified procapsids and capsids, respectively. Visualisation by negative stain TEM showed that the purified procapsids had a diameter of ~48 nm and appeared porous due to penetration of stain within their cores and were heterogenous (Fig. 1e), while the mature capsids were compact and impermeable to stain, with a diameter of ~42 nm (Fig. 1f). These morphologies are similar to those observed for the equivalent N $\omega$ V VLPs produced in insect cells<sup>13</sup>. For both procapsids and mature capsids, the yield of VLPs was in

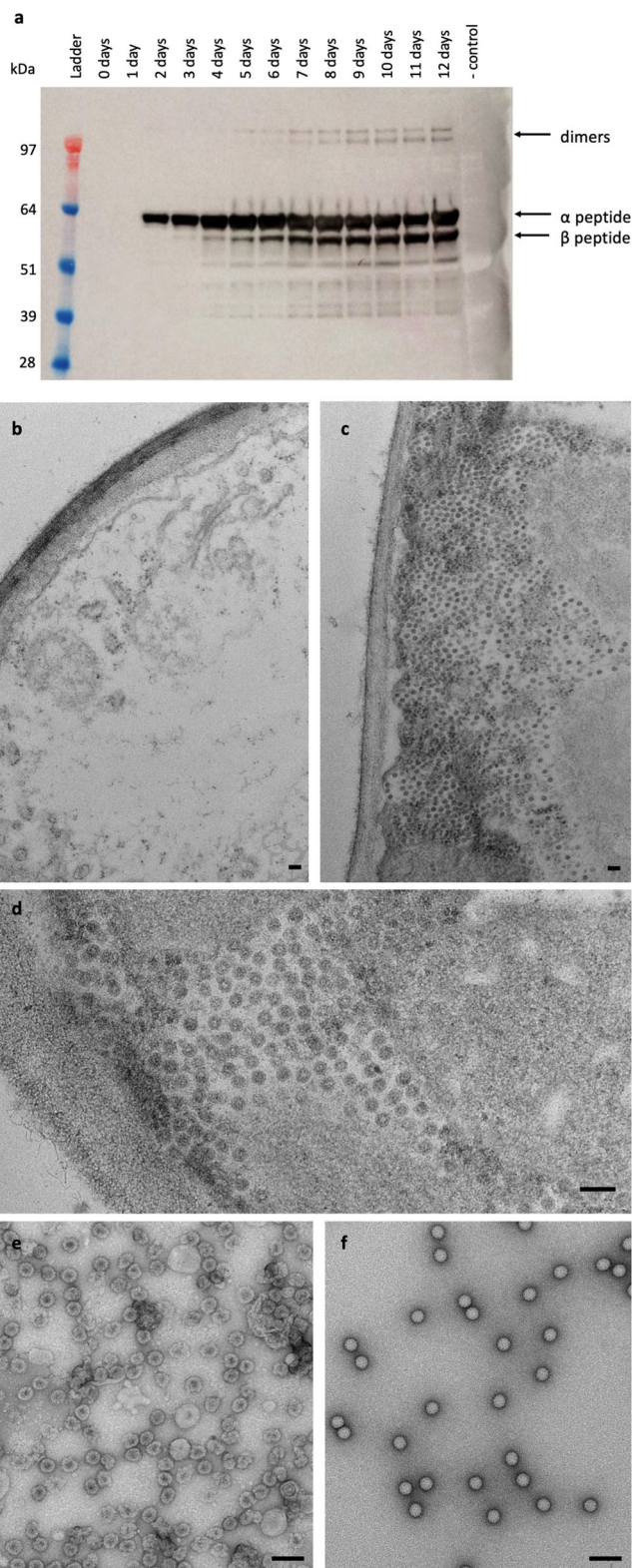


**Fig. 1 Expression of N $\omega$ V coat protein in *N. benthamiana*.** **a** Western blot of samples collected 0–12 dpi from leaves infiltrated with pEAQ-*HT*-N $\omega$ V-WT. The negative control (- control) was from leaf material infiltrated with pEAQ-*HT* (empty vector). The protein was detected using a polyclonal antibody for the N $\omega$ V coat protein. The positions of the uncleaved ( $\alpha$ ) and cleaved ( $\beta$ ) versions of the coat protein are indicated, as are the positions of the dimeric forms. Ladder = SeeBlue Plus 2 pre-stained protein standards. Electron micrographs of thin sections of leaves 3 dpi with pEAQ-*HT* (**b**) or pEAQ-*HT*-N $\omega$ V-WT at two different magnifications (**c**, **d**). All the leaf sections were counter-stained with 2% (w/v) uranyl acetate and 1% (w/v) lead citrate. Electron micrographs of purified procapsids (**e**) and capsids (**f**) negatively stained with 2% (w/v) uranyl acetate. For all micrographs the scale bar = 100 nm.

SDS-PAGE (Fig. 2a). This showed that cleavage occurred with a half-life of 45–60 min, compared with a half-life of 30 min for a sample of procapsids produced in insect cells that was analysed in parallel (Fig. 2b), the latter result being consistent with that reported previously<sup>26</sup>. Coat protein dimers also shifted in size, indicating that the dimerisation does not inhibit cleavage (Fig. 2a). As autocatalysis depends on the precise positioning of amino acids to a fraction of an Ångström<sup>27</sup>, this finding demonstrates the fidelity of N $\omega$ V VLP assembly in plants.

To assess the functionality of the  $\gamma$  peptide released during the pH-induced maturation of plant-produced procapsids in vitro, samples were mixed with DOPC liposome preparations at pH values from 5.0 to 9.0. As a control, VLPs produced in insect cells matured at pH 5.0 were analysed in parallel. These membrane disruption assays demonstrated that mature VLPs from both plants and insect cells have a similar lytic activity at alkaline pH (Fig. 3a). However, the plant-produced N $\omega$ V VLPs had a slightly higher initial rate of liposome lysis than the insect-cell produced particles (Fig. 3b).

**Structure analysis of N $\omega$ V VLPs.** N $\omega$ V procapsids purified from plants were analysed by cryo-electron microscopy. The particles were structurally heterogeneous, with many being broken or distorted (Fig. 1e and S3a), thereby limiting the resolution of the subsequent reconstruction. However, at 6.6 Å, the plant-produced procapsid model is the highest resolution structure of the N $\omega$ V procapsid currently available (Fig. 4a, c); the previously published N $\omega$ V procapsid structure being at only 28 Å resolution<sup>10</sup>.

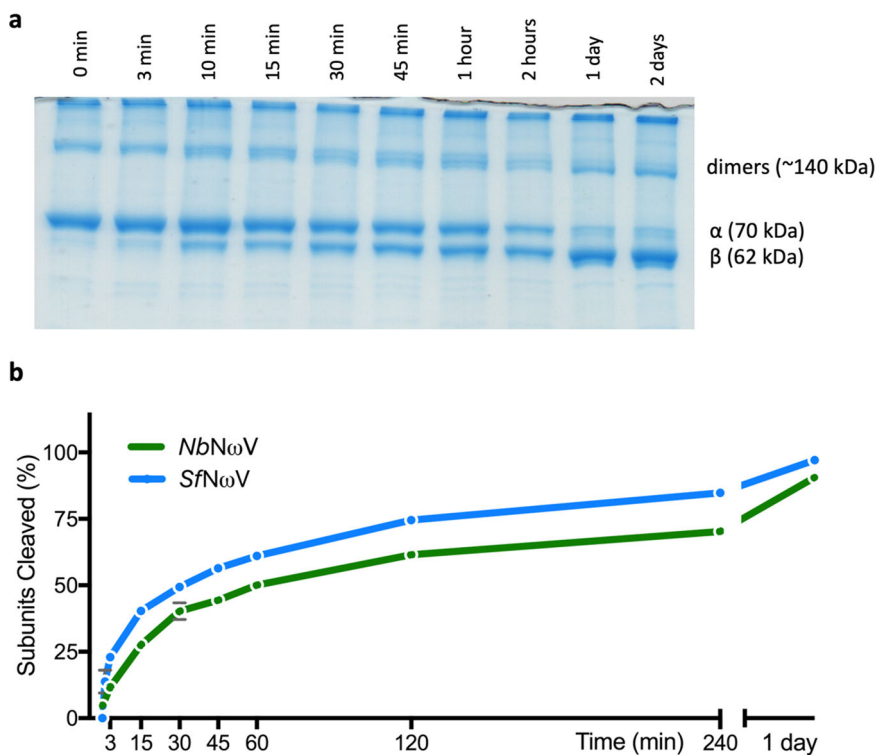
The more robust capsid VLPs (Figs. 2f and S3b) enabled a 3D reconstruction at 2.7 Å resolution, the highest resolution structure available for N $\omega$ V (Fig. 4b, d). Comparison with the 2.8 Å resolution crystal structure from authentic virions (PDB 1OHF) revealed that the virion and plant-expressed VLP capsids are virtually indistinguishable, with an rmsd in C $\alpha$  atoms of 0.461 Å between asymmetric units (ASU; based on 2256 aligned residues). Thus, this capsid structure demonstrates that N $\omega$ V VLPs produced in plants must initially assemble in a way that facilitates the authentic maturation pathway, and that plant-based expression systems are therefore able to support the complex maturation pathways of animal viruses.

Figure 5 shows the density of the procapsid (a) and capsid (b) rendered in colours that depict the 4 subunits in the icosahedral asymmetric unit; A (blue), clustered around the icosahedral five-fold axes and B (red), C (green) and D (yellow) clustered around the quasi-3-fold axes. Figure 5c, d show the change in density (viewed from inside the particle) between procapsid (c) and capsid (d) at the quasi-2-fold axes that relate an A, B, C trimer to the D, D, D trimer.

The model derived from the procapsid density was initially based on the rigid body fit of the jellyroll and Ig domains (residues 117–532) into the envelope of density that clearly

the range 0.1–0.25 mg of purified protein per gram of fresh weight infiltrated leaf tissue.

**Functional properties of plant-produced N $\omega$ V VLPs.** To determine whether the  $\alpha$  protein in plant-produced procapsids can undergo the autocatalytic cleavage associated with maturation in vitro, the pH of a suspension was rapidly reduced from pH 7.6 to pH 5.0 and the extent of  $\alpha$  protein cleavage monitored by



**Fig. 2 Autocatalytic cleavage analysis.** **a** SDS-PAGE analysis of plant-produced procapsids incubated for different times at pH 5.0. The positions of the uncleaved  $\alpha$  protein and the autoprocessed  $\beta$  protein are indicated as are the dimeric forms. **b** Comparison of the kinetics of cleavage of  $N\omega V$  procapsids from plants (green line) and insect cells (blue line). The fraction of subunits cleaved was determined by band densitometry of the stained gel image using the software ImageJ. A square of fixed size was used to delimit the gel area containing  $\alpha$  and  $\beta$  proteins. Each time point was measured individually, and the programme retrieved the density of each protein band. The sum of  $\alpha$  and  $\beta$  signals corresponded to 100%. Therefore, the extent of cleavage corresponds to the percentage of  $\beta$  density in relation to the total density of each time point. The raw data for the plot is given in Supplementary Data 1.

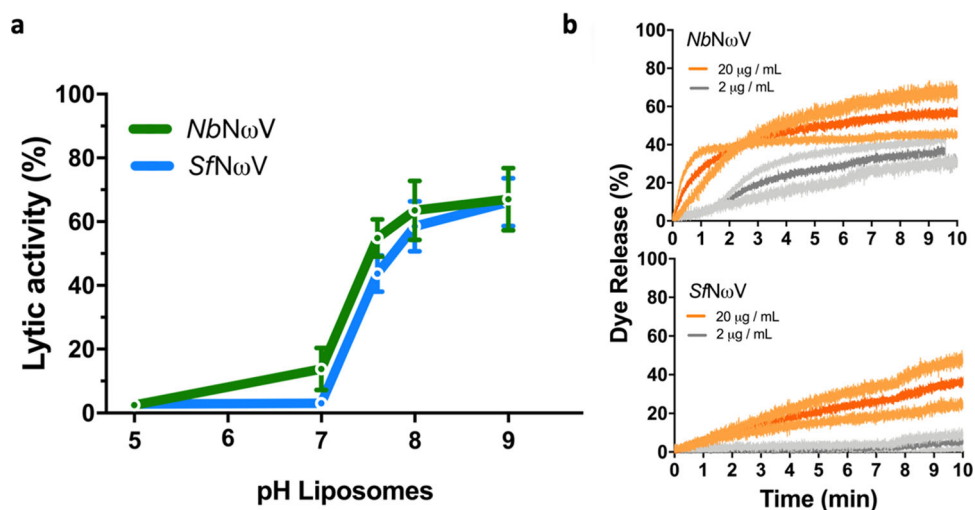


**Fig. 3 Membrane lytic activity of  $N\omega V$  VLPs produced in plants and insect cells.** **a** Lytic activity of mature  $N\omega V$  VLPs expressed in plants (green line) and insect cells (blue line) against DOPC liposomes under different pH conditions (from 5.0 to 9.0). End point values were measured after 10-min incubations with liposome preparations. Standard deviations from at least two experiments are shown as error bars. The raw data for the construction of the curves is given in Supplementary Data 2. **b** Initial kinetics of liposome dye release at pH 7.6 induced by mature  $N\omega V$  VLPs produced in plants (top panel) or insect cells (bottom panel). In each case, two  $N\omega V$  VLP concentrations were tested, 2  $\mu$ g/mL (grey lines) and 20  $\mu$ g/mL (orange lines). Standard deviations from at least two experiments are shown as lighter shades of each colour.

defined their positions and orientations in all four subunits within the icosahedral asymmetric unit. The N-terminal residues (44–116) and C-terminal residues (533–644), poorly defined in the previous procapsid reconstruction<sup>9</sup>, were modelled with approximate reference to the equivalent residues clearly defined

in the capsid. The modelling was aided by the equivalence of the density in the terminal regions in all four subunits of the procapsid, which is not the case in the capsid (Fig. 6). Treating the four subunit models as equivalent reduced the parameters and improved the confidence in the final coordinates.

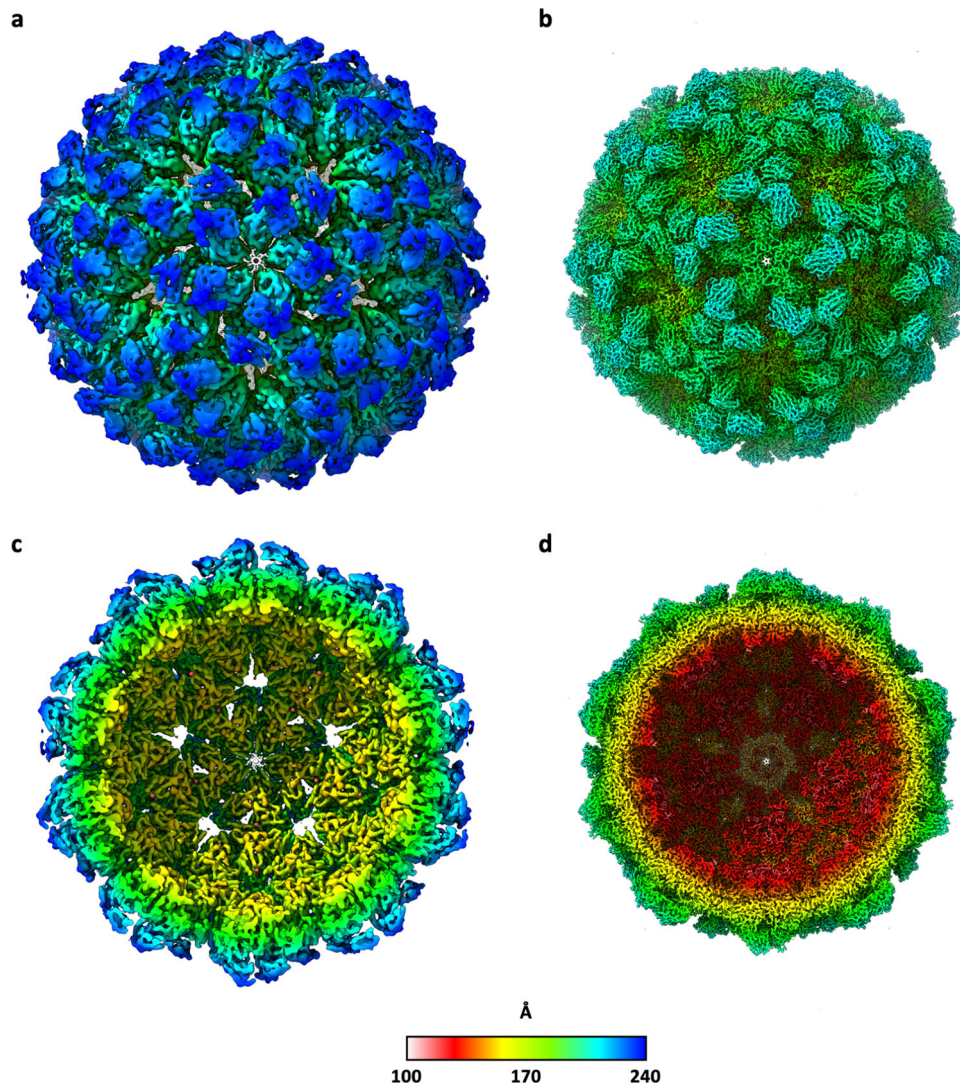


**Fig. 4** Radially coloured cryo-EM reconstructions of N $\omega$ V VLPs highlighting the degree of compaction on transitioning from the procapsid to the capsid. Full and cutaway views of the procapsid reconstruction at 6.6 Å resolution (**a**, **c**, respectively), and for the capsid at 2.7 Å resolution (**b**, **d**, respectively) are shown as viewed down the icosahedral five-fold axis. The surfaces are coloured with respect to the distance from the centre of each particle according to the key below.

## Discussion

The present study demonstrates that it is possible to recapitulate the complex maturation process involved in the production of N $\omega$ V VLPs in plants. While plants have previously been used to make capsids of viruses which require processing of the precursor protein by a viral protease, such as cowpea mosaic virus and poliovirus<sup>20,22</sup>, the production of a VLP that can undergo large-scale structural rearrangements and effect a precise autoproteolytic cleavage has not previously been demonstrated in plants, and so the results described here for N $\omega$ V are unique.

When the N $\omega$ V coat protein was expressed in plants, cleavage of the  $\alpha$  protein increased with the time that the particles remained in the plant. These results were unexpected since insect cell expression results exclusively in the production of procapsids, containing the uncleaved  $\alpha$  protein, when VLPs are purified at pH 7.6<sup>9,10</sup>, with cleavage only occurring upon acidification *in vitro*. The autocatalytic cleavage of non-enveloped virus coat proteins has usually evolved to occur in the extracellular environment, avoiding the generation of membrane-disruptive peptides inside the already-infected host cell<sup>28</sup>. The *in planta* maturation observed here could arise from acidification of the environment

over time. Although the pH of the plant cytoplasm is believed to be around 7.5, other compartments, such as the apoplast and vacuole, are more acidic<sup>29,30</sup>. Thus, tissue senescence could result in acidification of the environment where the VLPs accumulate. However, alternative explanations, such as an altered concentration of RNA in plant-expressed VLPs triggering maturation cannot be ruled out, as such a role for RNA has been found in the closely related tetra virus, *Helicoverpa armigera* stunt virus (HasV)<sup>31</sup>. Insect cell-expressed VLPs have been shown to contain host-derived RNA<sup>32</sup> and our preliminary results indicate that the plant-made VLPs also contain RNA, though this has not been characterised in detail.

Although the *in vitro* maturation and liposome lysis experiments demonstrate the biological functionality of plant-produced N $\omega$ V VLPs, some differences in the kinetics of both processes are apparent. The rate and efficiency of autocatalytic cleavage were both lower than found with those made in insect cells. By contrast, plant-derived particles have slightly higher initial lytic activity than insect-produced VLPs. These differences could be a consequence of differences in the dynamic properties of the particles produced in the two systems. One plausible cause of

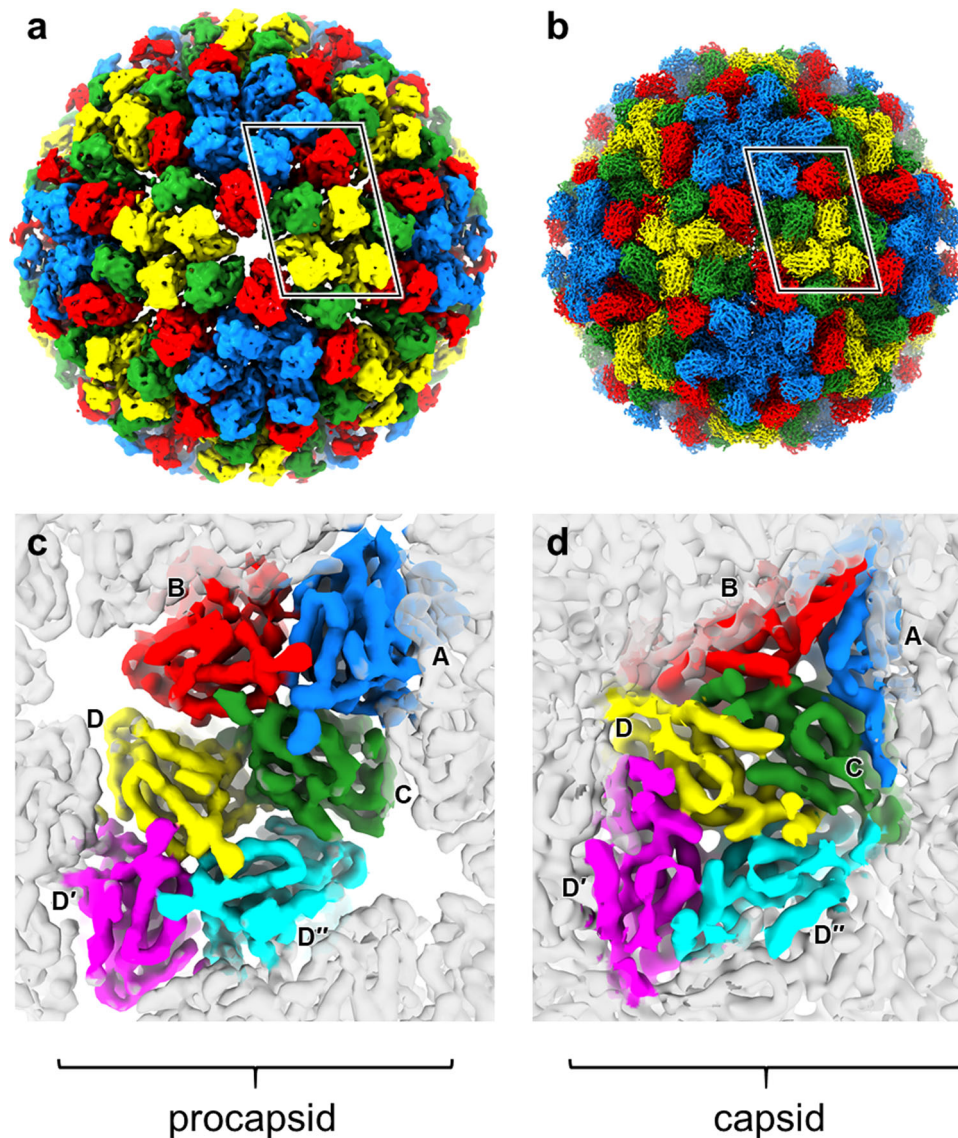


**Fig. 5 Cryo-EM reconstructions of NoV VLPs highlighting the quaternary structures.** Reconstructions of **a** the procapsid at 6.6 Å resolution and **b** the capsid at 2.7 Å resolution as viewed down the icosahedral two-fold axis. The density associated with four 70 kDa subunits that comprise the icosahedral asymmetric unit are coloured: A—blue, B—red, C—green and D—yellow. The highlighted region is shown below as viewed from the core of the particle for **c** the procapsid and **d** the capsid. The density for the rest of the particle is shown in semi-transparent grey. For ease of comparison the capsid density has been down-sampled to 6.6 Å resolution in **d**. In both the lower panels, subunits A–C are arranged around a quasi-three-fold axis and three copies of subunit D are arranged around the icosahedral three-fold axis (D—yellow; D'—magenta; D''—cyan; N.B. these are all yellow in **a, b**—different colours are used here to clearly define the densities associated with each subunit). Since icosahedral symmetry was imposed during reconstruction, the density associated with the three D-type subunits will be identical within each map. It is clear from these comparisons that the symmetry is very strong around the quasi-three-fold axis (A–C) in the procapsid but is broken in the capsid. Indeed, the subunit conformations and arrangements around the two types of three-fold axes are closely similar for the procapsid (A–C vs. D–D'). Additionally, these views highlight the porous packing seen in the procapsid relative to the highly compact arrangement of subunits in the capsid.

such changes could be the coat protein dimers that are present only in plant-derived particles; these could affect the efficiency of the quaternary rearrangements which accompany maturation. The alternative explanation, that the plant-produced samples contain a contaminant capable of lysing liposomes, is less likely as no lysis occurred when procapsids produced in plants were used in the assay.

We were able to solve the structure of plant-produced procapsids to 6.6 Å resolution and the structure of mature capsids to 2.7 Å resolution allowing comparison of the structures before and after maturation. The most dramatic aspect of the transition from procapsid to capsid is the ~30 Å translation-rotation of the

subunits from a maximum radius of 240 Å to the capsid radius of 210 Å. Due to the 6.6 Å resolution of the procapsid density and the remarkable correspondence when the density of the four subunit volumes was superimposed, in the refinement procedure structural equivalence was enforced on the four procapsid subunit models in the icosahedral asymmetric unit. The 2.7 Å resolution of the capsid allowed subunit models to be constructed and refined independently with no symmetry constraints within the icosahedral asymmetric unit. Figure 7 depicts the large-scale transitions graphically, with selected amino acids lying close to the geometric centres of the Ig, jellyroll and helical domains of the procapsid and capsid states and the vectors connecting these

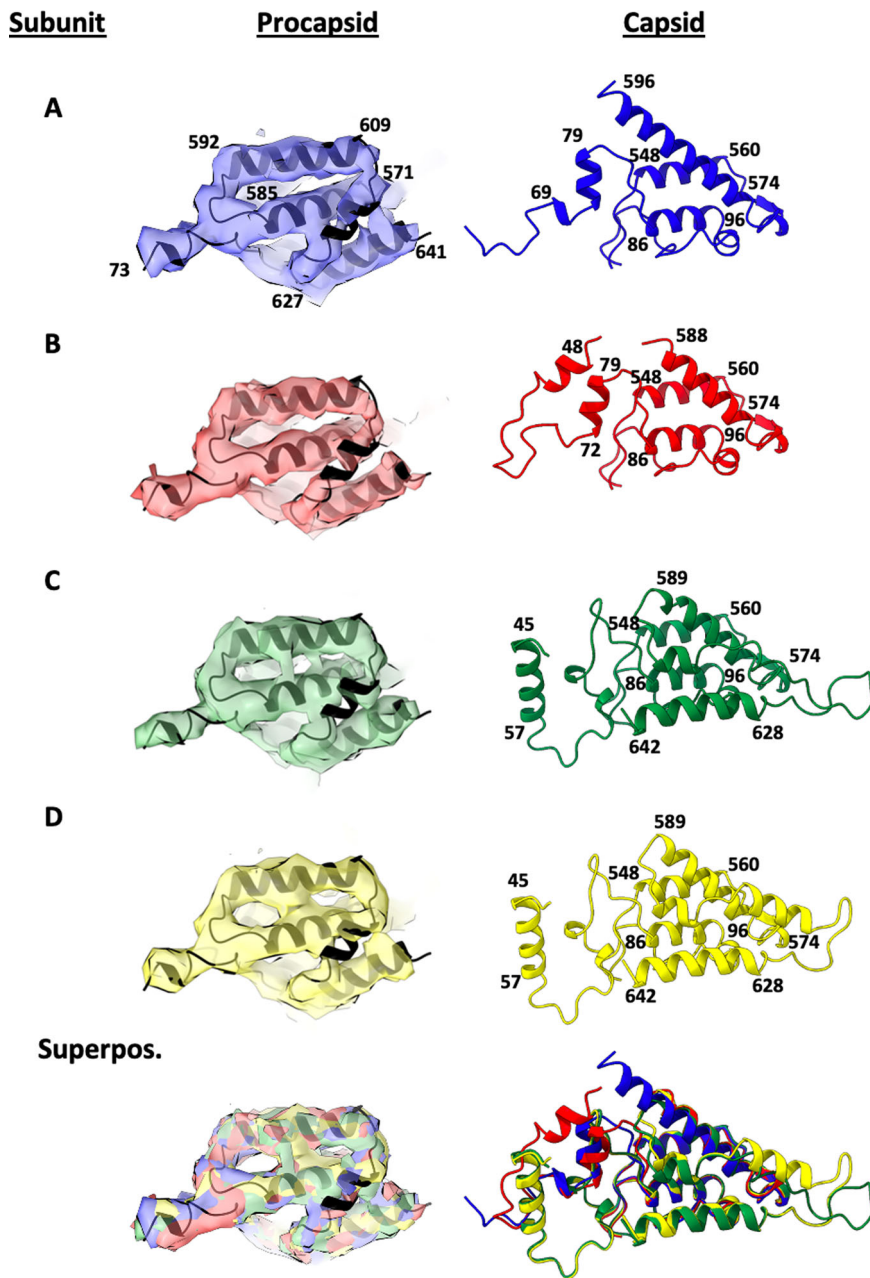


**Fig. 6 Internal helical domains of procapsid and capsid subunits in one icosahedral asymmetric unit.** Left: Procapsid cryo-EM density (6.6 Å resolution) and model for the internal helical domain (N-terminal and gamma peptide) of subunits A, B, C, D all viewed in the same orientation. The model of the internal helical domain (in black), refined as an identical rigid body for all four subunits, precisely fits the unique cryo-EM densities for the four subunits. Superposition of the four densities and models (bottom left) demonstrates the closely similar structures in this region of the procapsid. Right: Refined capsid models (2.7 Å resolution) of the internal helical domain in each of the four subunits and their superposition (bottom) reveals large differences from each other and the procapsid demonstrating substantial refolding of these sequences during maturation.

equivalent residues, being represented. Upon first inspection, the variations in vector lengths for the different subunit pairs (Fig. 7b, c) suggest that the domains move relative to one another and along different trajectories depending on the subunit type. However, a superposition of the four capsid subunit types onto the procapsid subunit reveals that equivalent marker atoms correspond closely in position. This shows that the relative placement of the three domains is essentially static and therefore the differences in the trajectory lengths between the subunit pairs mostly reflect different combinations of rigid body translations and rotations of the subunits rather than conformational rearrangements that are only seen in the helical region.

Regardless of the model interpretation in the procapsid, it is striking that the interior density in regions that must be occupied by the N and C terminal regions is virtually identical in all four subunits in the icosahedral asymmetric unit (Fig. 6). This is not the case in the capsid, demonstrating that subunits transition from being virtually equivalent in the initial procapsid assembly product to being non-equivalent in the capsid. This requires that, in addition to the large rigid body motions described above, the N and C-terminal regions that comprise the inner helical domain refold into different conformations despite having identical amino acid sequences. The refolding has two consequences obvious in the capsid structure. First, the active site for the



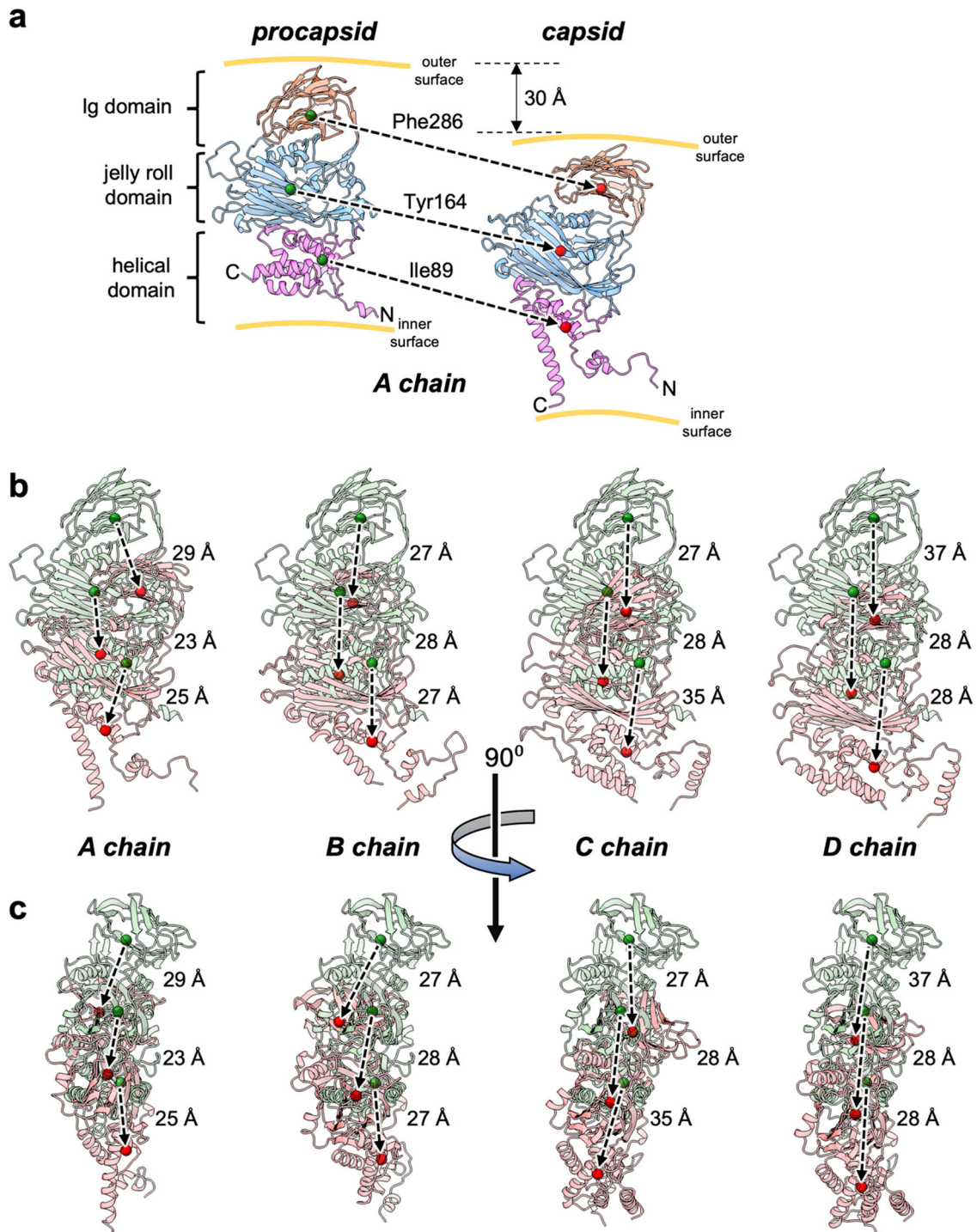


**Fig. 7 Trajectories of subunit motions on maturation from procapsid to capsid.** In addition to the significant refolding of the helical domain during capsid maturation, the N $\omega$ V subunits are translated through space by  $\sim 30$  Å as the protein coat contracts from a diameter of roughly 480 to one of 420 Å. To track the domain movements, we have defined three marker atoms that correspond to the C $\alpha$  atoms of equivalent residues in each subunit that lie close to the geometric centres of the three domains. **a** The protein backbone is shown as a semi-transparent cartoon and the marker atoms are shown as solid spheres (procapsid = green; capsid = red) with the three domains distinguished by different colours. For clarity in **(a)** only, the procapsid and capsid positions (for chain A only) have been separated horizontally, whereas in all the other panels their true relative positions are shown after superposition of the full procapsid and capsid icosahedra. For ease of comparison, in each of **(b, c)**, the subunit pairs have been oriented with respect to the same procapsid subunit view, with procapsid and capsid cartoons distinguished by green and red colouration, respectively. The trajectories of the marker atoms are indicated by dashed arrows. The large structural rearrangements in the helical domains occur mostly at the periphery where they interface with neighbouring subunits or form the inner surface of the particle; the core of this domain (including the marker atom) is essentially unchanged. Furthermore, superposition of all the capsid subunits onto the procapsid subunit reveals that equivalent marker atoms overlap closely. This indicates that the relative placement of the three domains remains effectively unchanged and therefore the differences in the trajectory lengths between the subunit pairs mostly reflect different combinations of rigid body translations and rotations of the subunits rather than conformational rearrangements.

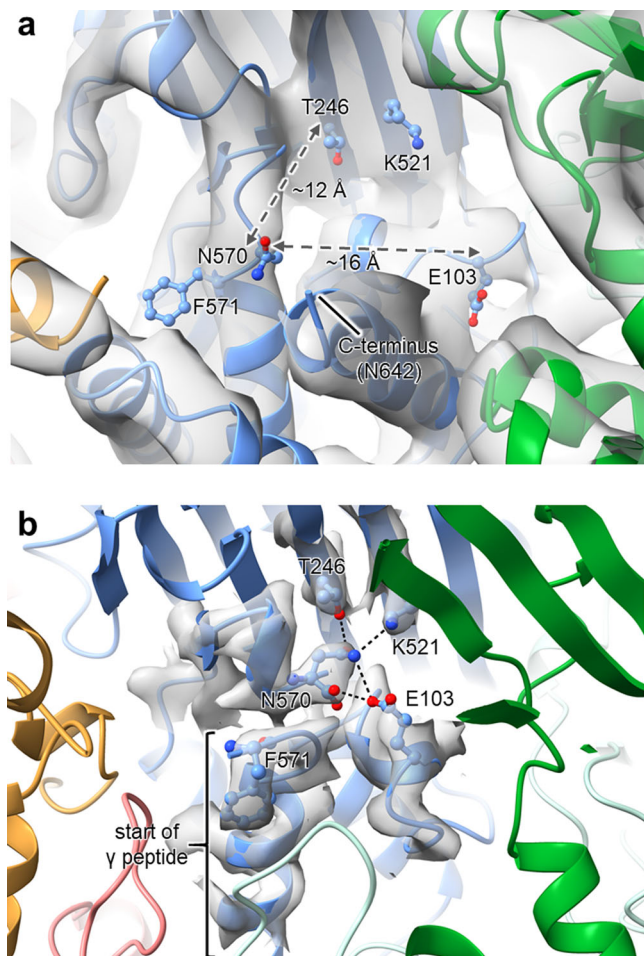


**Fig. 8 Structural remodelling at the NwV autocatalytic cleavage site.**

Close-up views of the cleavage site regions in the **a** procapsid and **b** capsid models revealing how disparate the key catalytic residues, Asn570 and Glu103, are in the procapsid as compared to their juxtaposition in the capsid following cleavage of the  $\gamma$  peptide (important residues are shown in ball-and-stick representation). For both models, the site in the A subunit is shown, which is coloured light blue, with neighbouring subunits depicted in different colours. Also shown are the density maps for the procapsid (6.6 Å resolution) and for the capsid (2.7 Å resolution), although for the latter, only the density associated with the highlighted residues is shown for clarity. Note that due to the low resolution of the procapsid reconstruction, the modelling of atomic coordinates is only approximate, especially for the protein side chains.

autocatalytic cleavage is formed in all subunits when the catalytic residue Glu 103 moves to function as a base for the formation of a cyclic imide and cleavage between residues Asn570 and Phe571 (Figs. 8a, b and S1). Since all the residues required for the cleavage are on the same polypeptide chain and cleavage does not occur in the procapsid, a refolding mechanism is the only way to create the active site. Second, residues 600–644 form extended helices in only the C and D subunits where they may function as a switch to promote the flat contacts between the C and D subunits related by quasi-2-fold axes and also to stabilise the particle (Fig. 5), though it is difficult to establish cause and effect from the analysis of two static structures. Indeed, the majority of the large structural rearrangements in the helical domains occur at the periphery where they interface with neighbouring subunits or form the inner surface of the particle. The procapsid structure provides new insights into the refolding required to achieve maturation and cleavage. Although much more detailed, the overall

description above supports the account by Canady et al.<sup>10</sup> comparing the procapsid structure (based on rigid body fitting of four capsid subunit models into the procapsid 28 Å cryo-EM density) and the mature virus structure. They proposed that the basic units of procapsid assembly are weakly interacting solution dimers that associate into weakly interacting trimers to form the fragile, spherical, procapsid structure of 240 virtually identical quasi-equivalent subunits. The fragility of the procapsid at neutral pH is due to electrostatic repulsions, allowing maturation to the infectious virion to be primed to occur when the pH is reduced to 5.0. During maturation, the subunits differentiate into tight trimers (the dominant morphological feature on the capsid surface) stabilised by the associated maturation cleavage. The newly determined procapsid structure reported here has allowed the molecular details of this process to be revealed. The stability of intermediates at different pH values suggests that the two-state system described here can be elaborated into a “movie” with the frames determined by the structures at different pH values.

## Materials and methods

**Plasmids.** The sequence encoding the NwV  $\alpha$  coat protein (Genbank MT875167), was codon optimised for *Nicotiana benthamiana* and synthesised by GeneArt (Life Technologies) with the flanking restriction sites AgeI and XhoI and a Kozak consensus sequence (TAACA) at the start of the coding sequence<sup>33</sup>. The gene was cloned into an AgeI/XhoI- digested pEAQ-HT plasmid<sup>24</sup> to produce pEAQ-HT-NwV. *Agrobacterium tumefaciens* LBA4404 were transformed with the construct by electroporation and bacterial suspension were infiltrated into plants as previously described<sup>23,25</sup>. For the production of NwV  $\alpha$  coat protein in insect cells, a pFastBac vector harbouring the NwV sequence (Genbank MT875167) was used with the Bac-to-Bac<sup>®</sup> Baculovirus Expression System (Invitrogen), as previously described<sup>16</sup>.

**Preparation and visualisation of leaf sections.** Infiltrated leaves were cut into 1 mm<sup>2</sup> fragments and fixed overnight in a solution of 2.5% (v/v) glutaraldehyde in 0.05 M sodium cacodylate, pH 7.3. Subsequent treatment was carried out as described by Meshcheriakova and Lomonosoff (2019)<sup>34</sup>. The leaf sections were counter-stained with 2% (w/v) uranyl acetate and 1% (w/v) lead citrate.

**Small-scale protein extraction.** Tissue agroinfiltrated with pEAQ-HT-NwV-WT was harvested at various days post-infiltration and samples of ~110–130 mg of fresh weigh material were immediately frozen in liquid nitrogen and then stored at –80 °C. The frozen leaf disks were ground and the powdered tissue was mixed with 200  $\mu$ l of extraction buffer (50 mM Tris, 250 mM NaCl, pH 7.6) + 100  $\mu$ l of 4 $\times$  NuPAGE LDS sample buffer (Invitrogen) containing  $\beta$ -mercaptoethanol (3:1 ratio) and immediately heated to 100 °C for 20 min. The samples were centrifuged at 16,000  $\times$  g for 30 min and the supernatant analysed on SDS-PAGE gels.

**Particle purification.** Leaves of *N. benthamiana* agroinfiltrated with pEAQ-HT-NwV were homogenised in two and a half volumes of extraction buffer (50 mM Tris, 250 mM NaCl, pH 7.6) using a waring blender. The crude extract was filtered through two layers of Miracloth (Millipore) and then centrifuged at 15,000  $\times$  g for 20 min at 11 °C. To purify procapsids, the supernatant was centrifuged through a 30% (w/v) sucrose cushion prepared in the same buffer as described by Peyret<sup>35</sup>. The resuspended pellets were clarified at 12,000  $\times$  g for 30 min at 11 °C and the supernatant was ultracentrifuged through 10–40% (w/v) continuous sucrose gradients. To purify mature capsids the clarified extracts were directly centrifuged through 10–50% (w/v) Optiprep gradients; 10–40% (w/v) sucrose gradients were also successfully used to produce mature capsids. In both cases the gradients were prepared in extraction buffer. Gradient fractions containing either procapsids or mature capsids were identified by SDS-PAGE, pooled and the samples further purified and concentrated using centrifugal filters (Amicon<sup>®</sup>, Merck) with a molecular weight cut-off (MWCO) of 100 kDa. The concentrated VLPs were stored in the fridge at 4 °C.

Purification of NwV VLPs produced in insect cells was performed as previously described<sup>16</sup>.

**SDS-PAGE and western blot analysis.** Protein extracts were analysed by electrophoresis on 4–12% (w/v) NuPAGE Bis-Tris gels (Life Technologies). The gels were either stained with Instant Blue (Expdeon) or the proteins transferred to nitrocellulose membranes for western blot analysis. Specific proteins were detected using an NwV polyclonal antibody raised in rabbits followed by detection with a goat anti-rabbit secondary antibody conjugated to horseradish peroxidase and developed using the chemiluminescent substrate Immobilon Western (Millipore).

**Table 1 Summary of cryo-EM data collection, processing and analysis.**

Data set	Procapsid	Capsid
Data collection and processing		
Microscope	Titan Krios	Titan Krios
Detector (mode)	Falcon III (integrating)	Falcon III (integrating)
Magnification	75,000 ×	75,000 ×
Magnified pixel size (Å)	1.065	1.065
Voltage (kV)	300	300
Total dose (e <sup>-</sup> /Å <sup>2</sup> )	72.0	79.5
Defocus range (µm)	-0.7 to -2.7	-0.8 to -3.0
Movies collected	8554	2788
Particle images	5426	21,395
Symmetry imposed	Icosahedral (I1)	Icosahedral (I1)
FSC threshold	0.143	0.143
Map resolution (Å)	6.63	2.72
Map resolution range (Å)	5.66-13.33	2.64-3.77
Refinement		
Initial model used (PDB code)	7ANM	1OHF
Map sharpening B factor (Å <sup>2</sup> )	-452.2	-125.0
Model composition (ASU)	Chains A, B, C, D	Chains A, B, C, D
Non-hydrogen atoms	17,464	17,518
Protein residues	2288	2290
R.m.s. deviations		
Bond lengths (Å)	0.005	0.006
Bond angles (°)	1.02	1.04
Validation		
EMRinger score	N/A <sup>a</sup>	5.1
Molprobrity score	2.93	1.59
Clashscore	22.45	4.06
Poor rotamers (%)	9.68	2.08
Ramachandran plot:		
Favoured (%)	95.2	97.1
Allowed (%)	4.8	2.9
Disallowed (%)	0.0	0.0
Ramachandran Z-score	1.02 ± 0.02	1.36 ± 0.02
Fit to map (CC <sub>mask</sub> )	0.74	0.88
Accession codes		
EMPIAR (dataset)	10555	10560
EMDB (maps)	11911	11830
PDB (model)	7ATA	7ANM

<sup>a</sup>The EMRinger score uses the density around side-chains to evaluate the fit of the protein backbone. At a resolution of 6.6 Å there is no discernible side-chain density and thus the EMRinger score is meaningless.

**Transmission electron microscopy of negatively stained particles.** Grids for negative staining were generated by applying 3 µl of sample (~0.1–1 mg/ml) on to carbon-coated 400 mesh copper grids (EM Resolutions). Prior to applying the sample, grids were glow-discharged for 20 s at 10 mA (Leica EM ACE200). Excess liquid was removed, and the grid was stained with 2% (w/v) uranyl acetate for 30 s. Grids were viewed using a FEI Tecnai G2 20 TWIN or FEI Talos 200 C TEM (FEI UK Ltd) at 200 kV and imaged using either an AMT XR-60 or OneView 4k × 4k digital camera (Gatan).

**Autocatalytic cleavage assays.** One volume of NøV procapsids suspended in 10 mM Tris-HCl, 250 mM NaCl, pH 7.6 was mixed with 9 volumes of 100 mM NaOAc, 250 mM NaCl, pH 5.0. The reactions were incubated at room temperature and stopped by adding protein loading buffer and immediately freezing the mixture with liquid nitrogen. The SDS-PAGE analysis was used to quantify cleavage by densitometry analysis of the stained gels as previously described<sup>26</sup>.

**Membrane disruption assays.** Liposomes composed of 1,2-dioleoyl-sn-glycero-3-phosphocholine (DOPC; Avanti Polar Lipids, Inc.) and containing sulforhodamine B (SulfoB; Invitrogen/Molecular Probes), a fluorescent dye, were prepared as previously described<sup>36</sup>. For the membrane disruption assays, the liposome suspensions in 10 mM HEPES buffer (pH 7.0) were diluted 100 × in the assay buffers: 100 mM Tris, 250 mM NaCl (adjusted to pH 7.5–9.5) or 100 mM sodium acetate, 250 mM NaCl (adjusted to pH 5.0–7.0). The initial fluorescence intensity of the liposome suspension was measured with a Cary Eclipse fluorescence spectrophotometer (Varian), with an excitation wavelength of 535 nm and an emission wavelength of 585 nm. When the reading was stable, the NøV procapsids or capsids were added to the liposome suspension to the required final concentration and incubated for 5–20 min at room temperature. During the incubation, the fluorescence intensity variations were recorded. Finally, Triton X-100 was added to the liposome suspension to a final concentration of 0.1% (v/v) to determine 100% dye release. The analysis of the data was performed as previously described<sup>16</sup>.

**Cryo-electron microscopy.** Cryo-EM grids were prepared by applying 3 µl of sample (~0.2–0.4 mg/ml) to 400 mesh copper grids with a supporting carbon lacey film (Agar Scientific, UK) held on an automatic plunge freezer (Vitrobot Mk IV). The lacey carbon was coated with an ultra-thin carbon support film, less than 3 nm thick (Agar Scientific, UK). Prior to applying the sample, grids were glow-discharged for 30 s (easiGlow, Ted Pella). The samples were vitrified by flash-freezing in liquid ethane, cooled by liquid nitrogen.

Data were collected on an FEI Titan Krios EM at 300 kV (Astbury Biostructure Laboratory, University of Leeds). The exposures were recorded using the EPU automated acquisition software on a FEI Falcon III direct electron detector. Micrographs were collected at a resolution of 1.065 Å/pixel. Movie stacks were motion-corrected and dose-weighted using MOTIONCOR2<sup>37</sup> (Fig. S3). CTF estimation was performed using GCTF<sup>38</sup> and particles were picked using RELION<sup>39,40</sup>. The autopicking was performed using 2D templates generated after an initial run without reference templates (Laplacian). Subsequent data processing was carried out using the RELION 2.1/3.0 pipeline<sup>39–41</sup> (Figs. S3 and S4) with the imposition of icosahedral symmetry for the 3D reconstructions. The capsid model was generated first, starting from the previously published crystal structure of the authentic virus (PDB entry 1OHF)<sup>42,43</sup>. The asymmetric unit (ASU), comprised of four protein chains, was rigid body fitted to the sharpened map in Chimera<sup>44</sup>. To expedite computation, for the subsequent steps, the ASU was visualised, manipulated and refined in the context of its eight nearest symmetry copies, denoted ASU8 (Fig. S5), and maps were cropped to cover just ASU8 with a 15 Å border using phenix.map\_box in PHENIX<sup>45</sup>. The model was edited using COOT<sup>46</sup> with reference to unsharpened and sharpened maps and refined using phenix.real\_space\_refine in PHENIX<sup>45</sup> against the latter. An updated ASU8 was generated from the central ASU after each refinement job. Validation of the final model was performed on the full capsid using Molprobrity<sup>47</sup> and EMRinger<sup>48</sup> through the PHENIX interface<sup>49</sup>. The final capsid model was used as the starting point for generating the model of the procapsid using a similar protocol. After sharpening in RELION, the resolution of the procapsid reconstruction was estimated to be 7.1 Å. However, after density modification with phenix.resolve\_cryo\_em in PHENIX<sup>50</sup> this increased to 6.6 Å, giving a concomitant improvement in the map quality, especially in regions where the structure was less well defined. Nevertheless, at this resolution, there was no discernible difference between the density for the subunits, thus non-crystallographic symmetry constraints were imposed to facilitate refinement, which was performed against the density improved map; Ramachandran restraints were also used. A summary of data collection, processing and analysis is given in Table 1 and rmsd values for pairwise superpositions of subunits from the NøV capsid and procapsid structures are shown in Table S1. Comparisons of cryo-EM densities around the quasi-three-fold and icosahedral three-fold axes of capsid and procapsid reconstructions are shown in Fig. S6. Structural figures were prepared using Chimera<sup>44</sup> and ChimeraX<sup>51</sup>.

**Reporting summary.** Further information on research design is available in the Nature Research Reporting Summary linked to this article.

## Data availability

The sequence of the NøV  $\alpha$  coat protein used in the study is available from Genbank Accession no. MT875167. All the data supporting the cryo-EM structural work have been deposited in the appropriate databases. Specifically, the raw data are available from EMPIAR (accessions 10555 and 10560), the reconstructions are available from EMDB (accessions 11911 and 11830), and the model coordinates are available from the PDB (accessions 7ATA and 7ANM). All data are freely available from the authors.

Received: 15 January 2021; Accepted: 20 April 2021;

Published online: 24 May 2021

## References

- Pornillos, O. & Ganser-Pornillos, B. K. Maturation of retroviruses. *Curr. Opin. Virol.* **36**, 47–55 (2019).
- Sirohi, D. & Kuhn, R. J. Zika virus structure, maturation, and receptors. *J. Infect. Dis.* **216**, S935–S944 (2017).
- Heymann, J. B., Conway, J. F. & Steven, A. C. Molecular dynamics of protein complexes from four-dimensional cryo-electron microscopy. *J. Struct. Biol.* **147**, 291–301 (2004).
- Kearney, B. & Johnson, J. Assembly and maturation of a T = 4 quasi-equivalent virus is guided by electrostatic and mechanical forces. *Viruses* **6**, 3348–3362 (2014).
- Johnson, J. E., Domitrovic, T., Matsui, T., Castells-Graells, R. & Lomonosoff, G. Dynamics and stability in the maturation of a eukaryotic virus: a paradigm for chemically programmed large-scale macromolecular reorganization. *Arch. Virol.* (2021) <https://doi.org/10.1007/s00705-021-05007-z>.

6. Hanzlik, T. N. & Gordon, K. H. J. The Tetraviridae. in *Advances in Virus Research* (eds. Maramorosch, K., Murphy, F. A. & Shatkin, A. J.) vol. 48 101–168 (Academic Press, 1997).
7. Speir, J. A. & Johnson, J. E. Tetraviruses. in *Encyclopedia of Virology 27–37* (Oxford: Elsevier, 2008).
8. Agrawal, D. K. & Johnson, J. E. Sequence and analysis of the capsid protein of *Nudaurelia capensis*  $\omega$  virus, an insect virus with T = 4 icosahedral symmetry. *Virology* **190**, 806–814 (1992).
9. Agrawal, D. K. & Johnson, J. E. Assembly of the T = 4 *Nudaurelia capensis*  $\omega$  virus capsid protein, post-translational cleavage, and specific encapsidation of its mRNA in a baculovirus expression system. *Virology* **207**, 89–97 (1995).
10. Canady, M. A., Tihova, M., Hanzlik, T. N., Johnson, J. E. & Yeager, M. Large conformational changes in the maturation of a simple RNA virus, *Nudaurelia capensis*  $\omega$  virus (N $\omega$ V). *J. Mol. Biol.* **299**, 573–584 (2000).
11. Matsui, T., Tsuruta, H. & Johnson, J. E. Balanced Electrostatic and Structural Forces Guide the Large Conformational Change Associated with Maturation of T = 4 Virus. *Biophysical J.* **98**, 1337–1343 (2010).
12. Canady, M. A., Tsuruta, H. & Johnson, J. E. Analysis of rapid, large-scale protein quaternary structural changes: time-resolved X-ray solution scattering of *Nudaurelia capensis*  $\omega$  virus (N $\omega$ V) maturation. *J. Mol. Biol.* **311**, 803–814 (2001).
13. Taylor, D. J., Krishna, N. K., Canady, M. A., Schneemann, A. & Johnson, J. E. Large-scale, pH-dependent, quaternary structure changes in an RNA virus capsid are reversible in the absence of subunit autoproteolysis. *J. Virol.* **76**, 9972–9980 (2002).
14. Banerjee, M. & Johnson, J. E. Activation, exposure and penetration of virally encoded, membrane-active polypeptides during non-enveloped virus entry. *Curr. Protein Pept. Sci.* **9**, 16–27 (2008).
15. Domitrovic, T. et al. Virus assembly and maturation: auto-regulation through allosteric molecular switches. *J. Mol. Biol.* **425**, 1488–1496 (2013).
16. Domitrovic, T., Matsui, T. & Johnson, J. E. Dissecting quasi-equivalence in nonenveloped viruses: membrane disruption is promoted by lytic peptides released from subunit pentamers, not hexamers. *J. Virol.* **86**, 9976–9982 (2012).
17. Dow, J. pH gradients in lepidopteran midgut. *J. Exp. Biol.* **172**, 355 (1992).
18. Byrne, M. J. et al. Combining transient expression and cryo-EM to obtain high-resolution structures of luteovirid particles. *Structure* **27**, 1761–1770 (2019). e3.
19. Castells-Graells, R., Lomonosoff, G. P. & Saunders, K. Production of Mosaic Turnip Crinkle Virus-Like Particles Derived by Coinfiltration of Wild-Type and Modified Forms of Virus Coat Protein in Plants. in *Virus-Derived Nanoparticles for Advanced Technologies: Methods and Protocols* (eds. Wege, C. & Lomonosoff, G. P.) 3–17 (Springer New York, 2018). [https://doi.org/10.1007/978-1-4939-7808-3\\_1](https://doi.org/10.1007/978-1-4939-7808-3_1).
20. Marsian, J. et al. Plant-made polio type 3 stabilized VLPs—a candidate synthetic polio vaccine. *Nat. Commun.* **8**, 245 (2017).
21. Marsian, J. et al. Plant-made nervous necrosis virus-like particles protect fish against disease. *Front. Plant Sci.* **10**, 880 (2019).
22. Saunders, K., Sainsbury, F. & Lomonosoff, G. P. Efficient generation of cowpea mosaicvirus empty virus-like particles by the proteolytic processing of precursors in insect cells and plants. *Virology* **393**, 329–337 (2009).
23. Thuenemann, E. C., Meyers, A. E., Verwey, J., Rybicki, E. P. & Lomonosoff, G. P. A method for rapid production of heteromultimeric protein complexes in plants: assembly of protective bluetongue virus-like particles. *Plant Biotechnol. J.* **11**, 839–846 (2013).
24. Sainsbury, F., Thuenemann, E. C. & Lomonosoff, G. P. pEAQ: versatile expression vectors for easy and quick transient expression of heterologous proteins in plants. *Plant Biotechnol. J.* **7**, 682–693 (2009).
25. Berardi, A., Castells-Graells, R. & Lomonosoff, G. P. High stability of plant-expressed virus-like particles of an insect virus in artificial gastric and intestinal fluids. *Eur. J. Pharm. Biopharm.* **155**, 103–111 (2020).
26. Matsui, T., Lander, G. & Johnson, J. E. Characterization of large conformational changes and autoproteolysis in the maturation of a T=4 virus capsid. *J. Virol.* **83**, 1126–1134 (2009).
27. Zlotnick, A. et al. Capsid assembly in a family of animal viruses primes an autoproteolytic maturation that depends on a single aspartic acid residue. *J. Biol. Chem.* **269**, 13680–13684 (1994).
28. Veesler, D. & Johnson, J. E. Virus maturation. *Annu. Rev. Biophys.* **41**, 473–496 (2012).
29. Martinière, A. et al. In vivo intracellular pH measurements in tobacco and arabidopsis reveal an unexpected pH gradient in the endomembrane system [W]. *Plant Cell* **25**, 4028–4043 (2013).
30. Martinière, A. et al. Uncovering pH at both sides of the root plasma membrane interface using noninvasive imaging. *Proc. Natl Acad. Sci. USA* **115**, 6488–6493 (2018).
31. Penkler, D. L. et al. Binding and entry of a non-enveloped T=4 insect RNA virus is triggered by alkaline pH. *Virology* **498**, 277–287 (2016).
32. Routh, A., Domitrovic, T. & Johnson, J. E. Host RNAs, including transposons, are encapsidated by a eukaryotic single-stranded RNA virus. *Proc. Natl Acad. Sci.* **109**, 1907–1912 (2012).
33. Castells-Graells, R. Viruses in motion: maturation of an insect virus-like particle – a nanomachine. Ph.D. thesis, University of East Anglia. (University of East Anglia - John Innes Centre, 2019).
34. Meshcheriakova, Y. & Lomonosoff, G. P. Amino acids at the exposed C-terminus of the S coat protein of cowpea mosaic virus play different roles in particle formation and viral systemic movement. *J. Gen. Virol.* **100**, 1165–1170 (2019).
35. Peyret, H. A protocol for the gentle purification of virus-like particles produced in plants. *J. Virol. Methods* **225**, 59–63 (2015).
36. Odegard, A. L. et al. Low endocytic pH and capsid protein autocleavage are critical components of flock house virus cell entry. *J. Virol.* **83**, 8628–8637 (2009).
37. Zheng, S. Q. et al. MotionCor2: anisotropic correction of beam-induced motion for improved cryo-electron microscopy. *Nat. Methods* **14**, 331–332 (2017).
38. Zhang, K. Gctf: Real-time CTF determination and correction. *J. Struct. Biol.* **193**, 1–12 (2016).
39. Scheres, S. H. W. RELION: Implementation of a Bayesian approach to cryo-EM structure determination. *J. Struct. Biol.* **180**, 519–530 (2012).
40. Zivanov, J. et al. New tools for automated high-resolution cryo-EM structure determination in RELION-3. *eLife* **7**, e42166 (2018).
41. Kimanius, D., Forsberg, B. O., Scheres, S. H. & Lindahl, E. Accelerated cryo-EM structure determination with parallelisation using GPUs in RELION-2. *eLife* **5**, e18722 (2016).
42. Helgstrand, C., Munshi, S., Johnson, J. E. & Liljas, L. The refined structure of *Nudaurelia capensis*  $\omega$  Virus reveals control elements for a T = 4 capsid maturation. *Virology* **318**, 192–203 (2004).
43. Munshi, S. et al. The 2.8 Å structure of a T=4 Animal virus and its implications for membrane translocation of RNA. *J. Mol. Biol.* **261**, 1–10 (1996).
44. Pettersen, E. F. et al. UCSF Chimera—A visualization system for exploratory research and analysis. *J. Comput. Chem.* **25**, 1605–1612 (2004).
45. Afonine, P. V. et al. Real-space refinement in PHENIX for cryo-EM and crystallography. *Acta Crystallogr. Sect. D. Struct. Biol.* **74**, 531–544 (2018).
46. Emsley, P., Lohkamp, B., Scott, W. G. & Cowtan, K. Features and development of Coot. *Acta Crystallogr. Sect. D. Biol. Crystallogr.* **66**, 486–501 (2010).
47. Williams, C. J. et al. MolProbity: more and better reference data for improved all-atom structure validation. *Protein Sci.* **27**, 293–315 (2018).
48. Barad, B. A. et al. EMRinger: side chain-directed model and map validation for 3D cryo-electron microscopy. *Nat. Methods* **12**, 943–946 (2015).
49. Afonine, P. V. et al. New tools for the analysis and validation of cryo-EM maps and atomic models. *Acta Cryst. D.* **74**, 814–840 (2018).
50. Terwilliger, T. C., Ludtke, S. J., Read, R. J., Adams, P. D. & Afonine, P. V. Improvement of cryo-EM maps by density modification. *Nat. Methods* **17**, 923–927 (2020).
51. Goddard, T. D. et al. UCSF ChimeraX: Meeting modern challenges in visualization and analysis: UCSF ChimeraX Visualization System. *Protein Sci.* **27**, 14–25 (2018).

## Acknowledgements

The authors thank Elaine Barclay and Kim Findlay for TEM training and assistance with TEM sample preparation, Maithe Vaslin de Freitas Silva for supplying plants and reagents in Brazil and Tsutomu Matsui for discussions on the biophysics of N $\omega$ V. We thank Matt Byrne and Tom Dendooven for helpful discussions about cryo-EM data processing. At the John Innes Centre, this work was supported by the United Kingdom Biotechnology and Biological Sciences Research Council (BBSRC) Synthetic Biology Research Center “OpenPlant” award (BB/L014130/1), the Institute Strategic Programme Grant “Molecules from Nature—Enhanced Research Capacity” (BBS/E/J/000PR9794), a capital grant award (BBSRC) to establish Cryo-EM capability at the John Innes Centre and the John Innes Foundation. The experiments done at Universidade Federal do Rio de Janeiro were supported by Conselho Nacional de desenvolvimento científico e tecnológico, CNPq; Fundação de Amparo à Pesquisa do Estado do Rio de Janeiro, FAPERJ. The Thermo-Fisher Titan Krios microscopes were funded by the University of Leeds (UoL ABSL award) and Wellcome Trust (108466/Z/15/Z).

## Author contributions

R.C.-G., J.R.S.R., E.L.H., C.A.S. and D.M.L. carried out the experiments and analysed data. G.P.L., J.E.J., T.D. and N.A.R. conceived and directed the project. All authors contributed to the writing and editing of the manuscript.

**Competing interests**

G.P.L. declares that he is a named inventor on granted patent WO 29087391 A1 which describes the HyperTrans expression system and associated pEAQ vectors used in this manuscript. All other authors declare no competing interests.

**Additional information**

**Supplementary information** The online version contains supplementary material available at <https://doi.org/10.1038/s42003-021-02134-w>.

**Correspondence** and requests for materials should be addressed to G.P.L.

**Reprints and permission information** is available at <http://www.nature.com/reprints>

**Publisher's note** Springer Nature remains neutral with regard to jurisdictional claims in published maps and institutional affiliations.



**Open Access** This article is licensed under a Creative Commons Attribution 4.0 International License, which permits use, sharing, adaptation, distribution and reproduction in any medium or format, as long as you give appropriate credit to the original author(s) and the source, provide a link to the Creative Commons license, and indicate if changes were made. The images or other third party material in this article are included in the article's Creative Commons license, unless indicated otherwise in a credit line to the material. If material is not included in the article's Creative Commons license and your intended use is not permitted by statutory regulation or exceeds the permitted use, you will need to obtain permission directly from the copyright holder. To view a copy of this license, visit <http://creativecommons.org/licenses/by/4.0/>.

© The Author(s) 2021